The Astrophysical Journal, 623:1–10, 2005 April 10
© 2005. The American Astronomical Society. All rights reserved. Printed in U.S.A.

CONSTRAINTS ON THE SMALL-SCALE POWER SPECTRUM OF DENSITY FLUCTUATIONS FROM HIGH-REDSHIFT GAMMA-RAY BURSTS

Andrei Mesinger
Department of Astronomy, Columbia University, 550 West 120th Street, New York, NY 10027

Rosalba Perna
JILA and Department of Astrophysical and Planetary Sciences, University of Colorado, Boulder, CO 80309-0391

and

Zoltán Haiman
Department of Astronomy, Columbia University, 550 West 120th Street, New York, NY 10027
Received 2004 December 25; accepted 2005 January 12

ABSTRACT

Cosmological models that include suppression of the power spectrum of density fluctuations on small scales exhibit an exponential reduction of high-redshift, nonlinear structures, including a reduction in the rate of gamma-ray bursts (GRBs). Here we quantify the constraints that the detection of distant GRBs would place on structure formation models with reduced small-scale power. We compute the number of GRBs that could be detectable by the *Swift* satellite at high redshifts ($z \gtrsim 6$), assuming that the GRBs trace the cosmic star formation history, which itself traces the formation of nonlinear structures. We calibrate simple models of the intrinsic luminosity function of the bursts to the number and flux distribution of GRBs observed by the Burst and Transient Source Experiment. We find that a discovery of high-z GRBs would imply strong constraints on models with reduced small-scale power. For example, a single GRB at $z \gtrsim 10$ or 10 GRBs at $z \gtrsim 5$ discovered by *Swift* during its scheduled 2 year mission would rule out an exponential suppression of the power spectrum on scales below $R_c = 0.09$ Mpc (exemplified by warm dark matter models with a particle mass of $m_x = 2$ keV). Models with a less sharp suppression of small-scale power, such as those with a red tilt or a running scalar index, n_s, are more difficult to constrain, because they are more degenerate with an increase in the power-spectrum normalization, σ_8, and with models in which star formation is allowed in low-mass minihalos. We find that a tilt of $\delta n_s \approx 0.1$ is difficult to detect; however, an observed rate of one GRB yr^{-1} at $z \gtrsim 12$ would yield an upper limit on the running of the spectral index, $\alpha \equiv dn_s/d\ln k > -0.05$.

Subject headings: cosmology: theory — dark matter — early universe — galaxies: formation — galaxies: high-redshift — gamma rays: bursts — large-scale structure of universe

1. INTRODUCTION

In the years leading up to the recent launch of the *Swift* satellite,[1] it has been increasingly recognized that distant gamma-ray bursts (GRBs) offer a unique probe of the high-redshift universe. In particular, GRBs are the brightest known electromagnetic phenomena in the universe and can be detected up to very high redshifts (e.g., Wijers et al. 1998; Lamb & Reichart 2000; Ciardi & Loeb 2000), well beyond the redshift $z \approx 6.5$ of the most distant currently known quasars (Fan et al. 2003) and galaxies (Kodaira et al. 2003).

There is increasing evidence that GRBs are associated with the collapse of short-lived, massive stars, including the association of bursts with star-forming regions (e.g., Fruchter et al. 1999), a contribution of supernova light to the optical afterglow (e.g., Bloom et al. 1999; Garnavich et al. 2003), and, most directly, association with a supernova (Stanek et al. 2003; Hjörth et al. 2003).

As a result, the redshift distribution of bursts should follow the mean cosmic star formation rate (SFR). Several studies have computed the evolution of the expected GRB rate under this assumption, based on empirical models of the global SFR (Totani 1997, 1999; Wijers et al. 1998; Lamb & Reichart 2000; Ciardi & Loeb 2000). Recent determinations of the cosmic SFR out to redshift $z \sim 5$ (e.g., Bunker et al. 2004; Gabasch et al. 2004; Giavalisco et al. 2004) show that star formation is already significant at the upper end of the measured redshift range, with $\gtrsim$10% of all stars forming prior to $z = 5$, which would result in a significant population of GRBs at these redshifts. Further associating star formation with the formation rate of nonlinear dark matter (DM) halos and using theoretical models based on the Press & Schechter (1974) formalism, Bromm & Loeb (2002) and Choudhury & Srianand (2002) extrapolated the SFR and obtained the GRB rates expected at still higher redshifts. These studies concluded that a significant fraction (exceeding several percent) of GRBs detected at *Swift*'s sensitivity should originate at redshifts as high as $z > 10$. The spectra of bright optical/IR afterglows of such distant GRBs could then reveal absorption features by neutral hydrogen in the intergalactic medium (IGM) and serve as an especially clean probe of the reionization history of the universe (Miralda-Escudé 1998; Lamb & Reichart 2000; Choudhury & Srianand 2002; Lamb & Haiman 2003; Barkana & Loeb 2004).

In this paper, we investigate a different method of using distant GRBs and gleaning information about early structure formation. The mere presence of a GRB at, say, $z > 10$ would indicate that nonlinear DM structures already exist at this redshift: the stars that give birth to the GRBs must form out of gas that collected inside dense DM potential wells. Structure formation in a cold dark matter (CDM)-dominated universe is "bottom up,'' with low-mass halos condensing first. In the current concordance cosmology, with densities in CDM and dark energy of $(\Omega_M, \Omega_\Lambda) \approx (0.3, 0.7)$ that have emerged from *WMAP* and other recent experiments (Spergel et al. 2003), DM halos with the masses of globular clusters (10^5–$10^6\ M_\odot$) condense from $\sim 3\ \sigma$ peaks of the initial primordial density field as early as $z \sim 25$. It is natural to identify these condensations as the sites where the first astrophysical objects, including the first massive stars, were born. As a result, one expects to possibly find GRBs out to this limiting redshift but not beyond.

---

[1] See http://swift.gsfc.nasa.gov.

With a scale-invariant initial fluctuation power spectrum, the CDM model has been remarkably successful and has matched many observed properties of large-scale structures in the universe and of the cosmic microwave background (CMB) radiation. However, the power spectrum on smaller scales, corresponding to DM halo masses of $M \lesssim 10^9\ M_\odot$, remains poorly tested. Recent observations suggest that the standard model predicts too much power on small scales: it predicts steep cusps at the centers of DM halos, whereas the rotation curves of dwarf galaxies suggest a flat core; it also predicts more small satellites than appear to be present in the Local Group (these and other problems with CDM on small scales are reviewed by, e.g., Sellwood & Kosowsky [2001] and Haiman et al. [2001]). Although astrophysical explanations of these observations are possible, much recent attention has been focused on solutions involving the properties of DM. Proposals include self-interacting DM (Spergel & Steinhardt 2000), a repulsive interaction to gravity (Goodman 2000; Peebles 2000), the quantum mechanical wave properties of ultralight DM particles (Hu et al. 2000), and a resurrection of warm dark matter (WDM) models (Bode et al. 2001).

By design, a common feature of models that attempt to solve the apparent small-scale problems of CDM is the reduction of fluctuation power on small scales. In addition, we note that reduced small-scale power is a direct consequence of a range of slow-roll inflationary models, which predict a red tilt of the power spectrum, $n_s \equiv d \ln P(k)/d \ln k < 1$, and a running of the spectral index $\alpha \equiv dn_s/d \ln k < 0$ (see, e.g., Kinney [2003] for a general discussion of power spectra predicted in different inflation models and Kosowsky & Turner [1995] for a discussion of models with a running index). Interest in such models was recently rekindled, as they appeared preferred by a combination of CMB anisotropy data from *WMAP* with fluctuation statistics in the Lyα forest (Spergel et al. 2003; Peiris et al. 2003).

The loss of small-scale power generically suppresses structure formation most severely at the highest redshifts, where the number of self-gravitating objects is drastically reduced. In each model, there exists a redshift beyond which the number of GRBs (or any other object) is exponentially suppressed, and a detection of a GRB beyond this redshift can be used to constrain such models. A similar constraint can be obtained from the observed reionization of the universe at high redshifts. For example, Barkana et al. (2001; hereafter BHO) showed that in the case of WDM models, invoking a WDM particle mass of $m_x \sim 1$ keV (approximately the mass required to solve the problems listed above), the paucity of ionizing sources makes it difficult to account for the reionization of the universe by redshift $z \sim 6$. Reionization as early as $z \sim 17$, as recently suggested by *WMAP* observations of CMB anisotropies (Spergel et al. 2003), would require extreme efficiencies for star formation and ionizing photon production for masses of $m_x \lesssim 2$ keV (see also Somerville et al. [2003], who reach similar conclusions).

GRBs, if discovered at $z > 6$, have the potential to provide independent and stronger constraints. *The purpose of this paper is to quantify the constraints that the detection of distant GRBs would place on structure formation models with reduced small-scale power.* Throughout most of our calculations, we focus on a WDM model as a proxy, but our results are valid for any theory that imposes a small-scale cutoff in the primordial power spectrum.

The rest of the paper is organized as follows. In § 2, we briefly describe our Monte Carlo approach to modifying the standard Press-Schechter formalism, allowing us to compute halo mass functions in WDM models. In § 3, we describe our method of computing the GRB rates using the halo mass functions, as well as simple models for the intrinsic GRB luminosity function. In § 4, we present the constraints that high-redshift GRB detections would place on the small-scale power spectrum. Finally, in § 5, we discuss the implications of this work and offer our conclusions.

Unless stated otherwise, throughout this paper we assume standard cosmological parameters $(\Omega_\Lambda,\ \Omega_M,\ \Omega_b,\ n,\ \sigma_8,\ H_0) = (0.73,\ 0.27, 0.044,\ 1,\ 0.85,\ 71\ \mathrm{km\ s^{-1}\ Mpc^{-1}})$, consistent with *WMAP* measurements of the CMB power spectrum on large scales (Spergel et al. 2003), and we quote all lengths in comoving units.

2. MASS FUNCTIONS IN CDM AND IN WDM

In this section, we briefly review the DM halo mass functions obtained in the Press & Schechter (1974; hereafter PS) and extended Press-Schechter (see Lacey & Cole 1993; hereafter EPS) formalisms, together with the modifications required to model structure formation in CDM models with reduced small-scale power. Our treatment closely follows that of BHO (which the reader is encouraged to consult for more details). In § 2.1, we describe the standard mass function, and in § 2.2, we motivate the parameterization of a power-spectrum cutoff in the WDM model. In § 2.3, we describe our Monte Carlo simulations needed to incorporate the additional effective pressure of the WDM particles with nonnegligible velocity dispersion. Readers not interested in the modeling details of the DM halos can skip directly to § 3, which describes how we associate GRBs with these halos.

2.1. *Halo Formation in CDM*

The mass function of DM halos in CDM models can be derived in closed form in the PS formalism. Although the PS mass function is in fair agreement with simulations, especially for the ''typical'' halos, it underestimates the number of rare, massive halos that are most relevant for our purposes; it also overestimates the number of low-mass halos when compared with large numerical simulations (e.g., Jenkins et al. 2001). Here we adopt a modified expression obtained by Sheth & Tormen (1999), which fits the simulated mass function to an accuracy of $\sim 10\%$,

$$\frac{dn(>M, z)}{dM} = -\frac{\langle\rho\rangle}{M}\frac{\partial[\ln \sigma(M)]}{\partial M}\sqrt{\frac{2}{\pi}}A\left(1+\frac{1}{\hat{\nu}^{2p}}\right)\hat{\nu}\exp\left(-\frac{\hat{\nu}^2}{2}\right). \tag{1}$$

Here dn/dM is the comoving number density of halos per unit mass, M is the total mass of the halo, $\langle\rho\rangle = \Omega_M \rho_{\mathrm{crit}}$ is the mean background matter density,

$$\sigma^2(M) = \int_0^\infty \frac{k^2\,dk}{2\pi^2} P(k)^2 W_k^2(M) \tag{2}$$

is the rms fluctuation in the mass enclosed within a region described by a top-hat filter in real space $W(M)$ (and its Fourier transform W_k), and $\hat{\nu} \equiv \sqrt{a}\delta_c(z)/\sigma(M)$, where a, p, and A are fitting parameters. Sheth et al. (2001) derive this form of the mass function by including shear and ellipticity in modeling nonlinear collapse, effectively changing the scale-free critical overdensity $\delta_c(z) \approx 1.68$, obtained in the case of spherically symmetric collapse (Peebles 1980), into a function of filter scale,

$$\delta_c(M, z) = \sqrt{a}\delta_c(z)\left\{1 + b\left[\frac{\sigma(M)}{a\delta_c^2(z)}\right]^c\right\}. \qquad (3)$$

Here b and c are additional fitting parameters (a is the same as in eq. [1]). We use this correction to obtain the critical threshold $\delta_c(M, z)$ from $\delta_c(z)$ [in the WDM case, $\delta_c(z)$ itself is modified as described in § 2.3 below]. For the constants in equations (1) and (3), we adopt the recent values obtained by Jenkins et al. (2001), who studied a large range in redshift and mass: $a = 0.73$, $A = 0.353$, $p = 0.175$, $b = 0.34$, and $c = 0.81$.

2.2. *Power Spectrum Cutoffs*

Structure formation in WDM matter models differs from that in CDM models in two main ways: (1) the free-steaming velocities of the particles wash out small-scale overdensities; (2) the residual particle velocities, although they redshift away as $1 + z$, create an effective "pressure," which slows the early growth of perturbations. Both effects suppress structure formation on small scales, but for the sake of generality we discuss the two effects separately. Free streaming is easily included computationally as a suppression of the power spectrum of fluctuations, and it is qualitatively similar, for example, to changes in the inflationary potential, which determines the power spectrum. Likewise, a red tilt of the power spectrum, $n_s \equiv d \ln P(k)/d \ln k < 1$, or a running of the spectral index, $\alpha \equiv dn_s/d \ln k < 0$, is easily included in the analysis by simply modifying the power spectrum in equation (2). On the other hand, the effective pressure in WDM models is more difficult to include computationally and is specific to the WDM model; it is discussed separately in the next subsection.

Free streaming manifests itself as a cutoff in the power spectrum, which "flattens" $\sigma(M)$ for small M. This effect becomes more severe as the WDM particle mass is lowered, as demonstrated in the bottom panel of Figure 1 for $m_x = 2$ and 1 keV. To produce a given energy density contribution, Ω_x (where we take $\Omega_x \equiv \Omega_M - \Omega_b$), the required WDM particle mass is determined by $m_x n_x \propto \Omega_x h^2$, where the present number density, n_x, follows from the particle distribution function. This can be used (see BHO) to relate the particle mass and the rms velocity dispersion, $v_{\rm rms}$:

$$v_{\rm rms}(z) = 0.0437(1 + z)\left(\frac{\Omega_x h^2}{0.15}\right)^{1/3}\left(\frac{g_x}{1.5}\right)^{-1/3}\left(\frac{m_x}{1\ {\rm keV}}\right)^{-4/3}, \qquad (4)$$

where g_x is the effective number of degrees of freedom of WDM. The usual assumption of a fermionic spin-$\frac{1}{2}$ particle yields $g_x = 1.5$. This modifies the CDM power spectrum (which we take from Eisenstein & Hu 1999) by multiplying it with the square of a transfer function (Bode et al. 2001):

$$T_x(k) = \left[1 + (\epsilon k R_c)^{2\nu}\right]^{-\eta/\nu}, \qquad (5)$$

with parameters $\epsilon = 0.361$, $\eta = 5$, and $\nu = 1.2$. The power spectrum is reduced to half its value in CDM at $k = 1/R_c$, at which the cutoff scale, R_c, is given by

$$R_c = 0.201\left(\frac{\Omega_x h^2}{0.15}\right)^{0.15}\left(\frac{g_x}{1.5}\right)^{-0.29}\left(\frac{m_x}{1\ {\rm keV}}\right)^{-1.15}, \qquad (6)$$

where R_c is in comoving megaparsecs. Here, we only consider particles with fermionic spins, i.e., $g_x = 1.5$, but all results can be scaled for arbitrary values of g_x using the equation above. The corresponding mass scale, $M_c = (4/3)\pi R_c^3 \langle\rho\rangle$, is

$$M_c = 1.74 \times 10^8\left(\frac{\Omega_M h^2}{0.15}\right)\left(\frac{R_c}{0.1\ {\rm Mpc}}\right)^3 M_\odot. \qquad (7)$$

We will use R_c and m_x interchangeably, with equation (6) relating them.

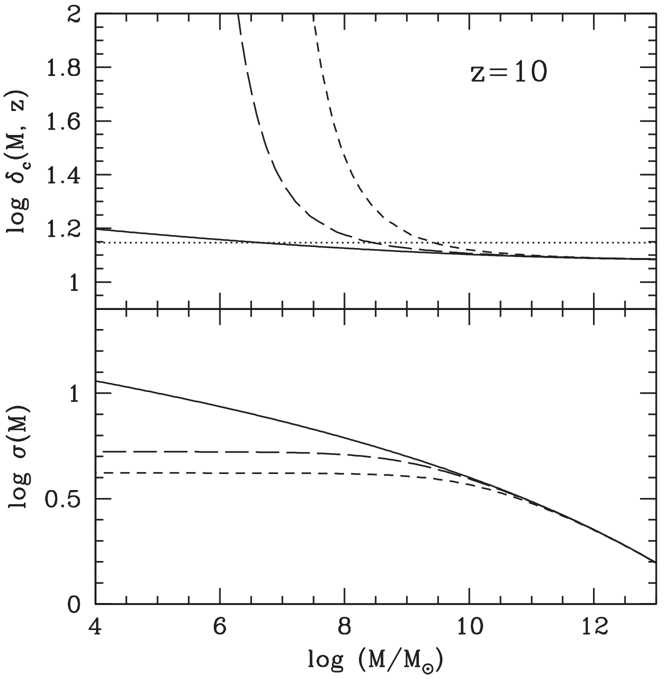

FIG. 1.—*Top*: Critical overdensity threshold as a function of scale, evaluated for $z = 10$. The dotted curve represents the scale-free critical overdensity $\delta_c(z)$. The solid curve corresponds to CDM, the long-dashed curve to a WDM particle mass of $m_x = 2$ keV, and the short-dashed curve to $m_x = 1$ keV. All curves incorporate the correction from eq. (3), except for the dotted curve. *Bottom*: The rms mass fluctuation in top-hat filters of mass scale M. As above, the solid curve corresponds to CDM, the long-dashed curve to $m_x = 2$ keV (or power-spectrum cutoff scale $R_c = 0.087$ Mpc), and the short-dashed curve to $m_x = 1$ keV (or $R_c = 0.193$ Mpc).

2.3. *Effective Pressure of WDM Particles*

As mentioned above, structure formation in WDM models is further suppressed by the residual velocity dispersion of the WDM particles, which delay the growth of perturbations. We use the results of BHO, who made an analogy with an ideal gas whose temperature corresponds to the velocity dispersion of the WDM. In this case, the pressure delays the collapse and can be effectively included in the mass function computed in the EPS analysis by raising the critical linear extrapolated overdensity threshold at collapse $\delta_c(z)$. BHO computed the critical overdensity by following the collapse of spherical perturbations, using a one-dimensional, spherically symmetric Lagrangian hydrodynamics code originally developed by Thoul & Weinberg (1996).

The top panel in Figure 1 shows δ_c (adopted from BHO) as a function of M, at the fixed redshift $z = 10$. The dotted curve represents the scale-free critical overdensity $\delta_c(z)$ arising from spherical collapse. The solid curve corresponds to CDM, the long-dashed curve to WDM with $m_x = 2$ keV, and the short-dashed curve to $m_x = 1$ keV. The threshold is found to increase sharply below the mass scale

$$M_{\rm J} = 3.06 \times 10^8 \left(\frac{g_x}{1.5}\right)^{-1} \left(\frac{\Omega_x h^2}{0.15}\right)^{1/2} \times \left(\frac{m_x}{1\ \rm keV}\right)^{-4} \left(\frac{1+z_i}{3000}\right)^{3/2} M_\odot, \qquad (8)$$

which can be shown (see BHO) to correspond to an analog of a "Jeans mass," i.e., the scale of the objects whose collapse is significantly delayed by the pressure.

Since $\delta_c(M, z)$ is a function of scale in WDM models, one cannot obtain WDM mass functions from the standard EPS analysis, which uses the symmetry in the random walk trajectories of δ versus M about a fixed threshold (Lacey & Cole 1993). Instead, we compute the mass functions using Monte Carlo simulations. We generate random realizations of trajectories $\delta(M)$, as the scale is decreased from $M \sim \infty$, and generate the histograms of the scales at which the trajectory first crosses the $\delta_c(M, z)$ threshold. Each step in the random walk, $\Delta\delta(M)$, is Gaussian distributed with a variance of $\sigma^2_{\rm step}(M, \Delta M) = \sigma^2(M) - \sigma^2(M - \Delta M)$. When constructing such a random walk, one must be careful to use steps small enough such that as the smoothing scale M is decreased by ΔM, the likelihood that the $\delta_c(M, z)$ threshold is crossed between M and $M - \Delta M$ is small. The physical reason for this is the so-called cloud-in-cloud problem: to ensure that we do not step over a collapsed halo as we decrease the smoothing scale M [i.e., that our $\delta(M)$ trajectory has not gone above $\delta_c(M, z)$ and then dropped below it again within the range ΔM]. We use an adaptive step size, set so that the barrier $\delta_c(M, z)$ is at least 7 $\sigma_{\rm step}$ away from $\delta(M)$, with a minimum resolution of $\Delta M = M/100$. Formally, defining $\Delta_7 M$ such that $[\delta_c(M, z) - \delta(M)]/\sigma_{\rm step}(M, \Delta_7 M) = 7$, our step size is $\Delta M = {\rm MAX}(M/100,\ \Delta_7 M)$. We find that these parameters efficiently reproduce the standard EPS mass function in the CDM case to an accuracy of a few percent.

We also find that a starting mass for the random walk trajectories as small as $\sim 10^{16}\ M_\odot$ is sufficient to obtain accurate mass functions at $z = 0$. The starting mass can be decreased as redshift increases, since the characteristic mass that is collapsing gets smaller as redshift increases. A starting mass of $\sim 10^{12}\ M_\odot$ is sufficient at $z = 15$.

The number of simulated trajectories required to obtain accurate mass functions is a strong function of redshift. This is to be expected, since virialized structure becomes very rare at high redshift. We show this effect in Figure 2, where we plot the fraction of the total mass collapsed into halo of mass M or higher, $F(>M, z)$, as a function of redshift. The shaded region shows the collapsed fraction in CDM, with a range of low-mass cutoffs corresponding to virial temperatures 300 K $< T_{\rm vir} < 10^4$ K (see discussion in § 3 below). The other curves correspond to WDM particle masses of $m_x = 3.0$, 2.5, 2.0, 1.5, 1.0, and 0.5 keV (*top to bottom*) and do not assume any low-mass threshold (effectively, $M = 0$). Introducing the same two low-mass cutoffs as in the CDM case would leave the WDM results essentially unchanged, since the power is already strongly suppressed in excess of these cutoffs at the high redshifts where these low-mass halos would dominate the collapse fraction (see the discussion below or Fig. 7 in BHO). As can be seen, simulating high-redshift mass functions for small particle masses can be prohibitively expensive computationally. For example, we find that accurate mass functions for $m_x < 1$ keV at $z > 15$ require $\gtrsim 10^9$ Monte Carlo runs, as less than one in a million $\delta(M)$ trajectories crosses $\delta_c(M, z)$.

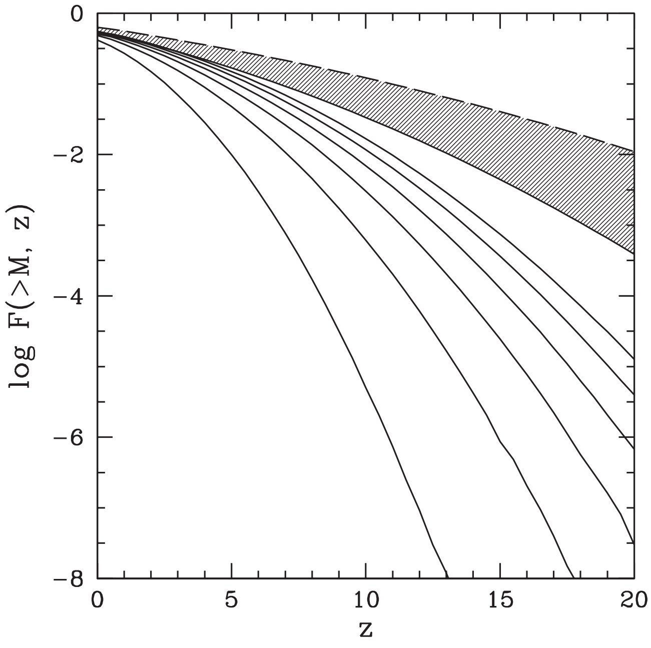

FIG. 2.—Fraction of the total mass collapsed into halos of mass M or greater, $F(>M, z)$, as a function of redshift. The shaded region shows the collapsed fraction in CDM, with a range of low-mass cutoffs corresponding to virial temperatures 300 K $< T_{\rm vir} < 10^4$ K. The other curves correspond to WDM particle masses of $m_x = 3.0$, 2.5, 2.0, 1.5, 1.0, and 0.5 keV (*top to bottom*) and do not assume any low-mass threshold (effectively, $M = 0$). The cutoffs used in the CDM case would leave the WDM results essentially unchanged (see discussion in text).

Figure 3 shows sample cumulative mass functions at redshifts $z = 10$ (*top*) and $z = 15$ (*bottom*). The solid curves correspond to CDM; the dotted curves correspond to WDM models with $m_x = 2$ and 1 keV (*top to bottom*). The dashed curves are mass functions for the same two WDM models but incorporate only a power-spectrum cutoff, ignoring the effective pressure of WDM. The WDM mass functions were created with 10^9 Monte Carlo runs as explained above. [Note that our results are slightly different from those of BHO; this is due to a small correction to BHO's derivation of R_c and the corresponding $\sigma(M)$.]

As can be seen from Figure 3, including the pressure term in the WDM models further suppresses the number of halos relative to the models that include only the power-spectrum cutoff. Furthermore, the relative importance of the pressure term increases with increasing redshift. As anticipated, the overall differences between the WDM and CDM mass functions increase toward higher redshift. This is because in the early universe, the characteristic scale of collapsing and virializing halos was smaller and closer to the cutoff scales discussed above. These large differences aid in discriminating between models with different power-spectrum cutoff scales.

3. THE EVOLUTION OF THE GRB RATE WITH REDSHIFT

In this section, we describe a model for the expected evolution in the rate of all GRBs, as well as the fraction that can be

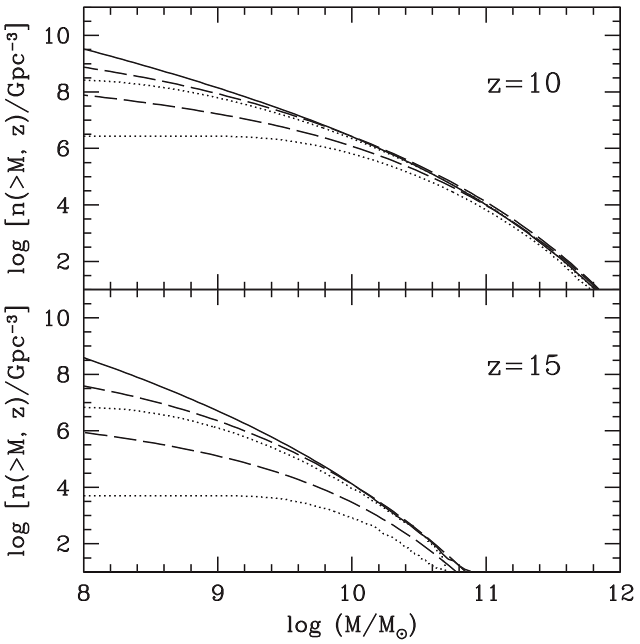

FIG. 3.—Cumulative mass functions (number of halos with masses greater than M Gpc^{-3}) at redshifts $z = 10$ (*top*) and $z = 15$ (*bottom*). The solid curves show mass functions in CDM models; the dotted curves correspond to WDM models with $m_x = 2$ and 1 keV (*top to bottom*); the dashed curves are mass functions in the same two WDM models, but incorporating only a power spectrum cutoff (§ 2.2) and no WDM pressure (§ 2.3). The WDM cumulative mass functions were created with 10^9 Monte Carlo realizations of $\delta(M)$ trajectories.

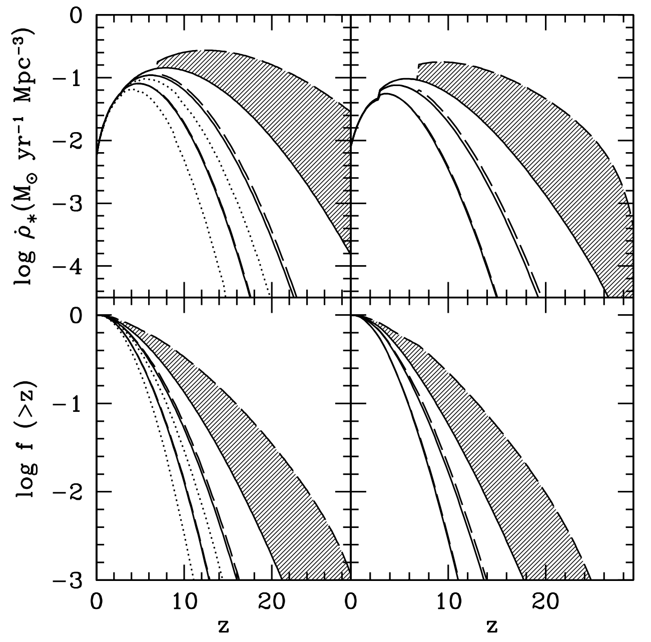

FIG. 4.—*Top*: SFR densities assuming instantaneous star formation in a collapsing halo (*left*) and a finite exponential spread in star formation times (*right*). The solid curves assume a minimum virial temperature $T_{\rm vir} = 10^4$ K of a halo for star formation and include the effect of power-spectrum suppression below various cutoff scales: $R_c = 0$ Mpc ($m_x \to \infty$; i.e., standard CDM), $R_c = 0.193$ Mpc ($m_x = 1$ keV), and $R_c = 0.087$ Mpc ($m_x = 2$ keV) (*top to bottom*). The dashed curves assume a minimum temperature, $T_{\rm vir} = 300$ K, with the same cutoff scales. The dotted curves correspond to models that include the additional effect of the effective pressure of WDM particles with mass $m_x = 2$ and 1 keV (*top to bottom*). The shaded area highlights the expected range in SFR densities in CDM models with minimum virial temperatures 300 K $\lesssim T_{\rm vir} \lesssim 10^4$ K. *Bottom*: Fraction of all GRBs that originate at redshifts higher than z in the models corresponding to the top panels.

detected by *Swift*. As is commonly done in the context of predicting the rate of GRBs at high redshift (Bromm & Loeb 2002; Choudhury & Srianand 2002), we assume that the GRB rate density (the number of GRBs per unit time per unit comoving volume), $\dot{\rho}_{\rm GRB}(z)$, is proportional to the global SFR density,

$$\dot{\rho}_{\rm GRB}(z) \approx K\dot{\rho}_*(z), \tag{9}$$

where K is the proportionality constant in units of $M_\odot^{-1}$, and $\dot{\rho}_*(z)$ is the stellar mass produced on average per unit comoving volume per unit time. First we discuss the evolution of the SFR and then the normalization of the corresponding GRB rate. In § 3.1.2 we discuss the uncertainties of our approach.

3.1. *Star Formation Rate in Halos*

We estimate the global SFR density at redshift z as

$$\dot{\rho}_*(z) = \epsilon_* \frac{\Omega_b}{\Omega_M} \int_{M_{\rm min}}^{\infty} dM \int_{\infty}^{z} dz' M \frac{\partial^2 n(>M, z')}{\partial M \partial z'} P(\tau), \tag{10}$$

where ϵ_* is the efficiency parameter for the conversion of gas into stars, $M\, dM\, \partial n(>M, z')/\partial M$ is the mass density contributed by halos with masses between M and $M + dM$ at redshift z, $t(z)$ is the age of the universe at redshift z, and $P(\tau)$ is the probability per unit time that new stars form in a mass element of age $\tau \approx t(z) - t(z')$. We adopt the fiducial value of $\epsilon_* = 0.1$ (see, e.g., Cen 2003), but note that our results are insensitive to this value, since we normalize the coefficient K in order to match our total GRB rate with observations (the important assumption is only that ϵ_* is constant; this assumption is probably conservative, as discussed below). We also note that the simple time derivative of the halo mass function in equation (10), in general, contains a contribution from mergers between halos, in addition to the formation of new halos (see, e.g., Sasaki [1994] for a discussion). However, the integral in equation (10) is sensitive only to the total virialized mass above mass $M_{\rm min}$, so that this ambiguity should not affect our results (although we note that the formation of new halos dominates in our case, since the relevant halos are above the nonlinear mass scale).

The minimum mass, $M_{\rm min}$, depends on the efficiency of gas cooling and collapsing into a DM halo. Without molecular hydrogen, $M_{\rm min}$ corresponds to a halo with virial temperature, $T_{\rm vir} \sim 10^4$ K; with H$_2$, $T_{\rm vir} \sim 300$ K (Haiman et al. 2000; we use the conversion between halo mass and virial temperature as given in Barkana & Loeb 2001). The amount of H$_2$ present in the early universe is uncertain, so below we present results for both $T_{\rm vir} > 10^4$ K and $T_{\rm vir} > 300$ K. We note that only the CDM mass functions are sensitive to these cooling thresholds (see Fig. 4). In our models that incorporate small-scale power suppression, as the characteristic collapse scale approaches the cooling cutoff, $T_{\rm vir}$, the cooling cutoff has already become smaller than the power-spectrum cutoff, R_c. Hence, we do not distinguish between models with $T_{\rm vir} > 10^4$ K and $T_{\rm vir} > 300$ K for the WDM particle masses presented below.

In the presence of an ionizing background, the cosmological Jeans mass, above which gas can collect in DM halos, is increased, corresponding to virial temperatures $\gtrsim 10^4$ K (Rees 1986; Efstathiou 1992). Early work on this subject (Thoul & Weinberg 1996) suggested that an ionizing background would completely suppress star formation in halos with circular velocities $v_{\rm circ} \lesssim 35$ km s^{-1} and partially suppress star formation in halos with 35 km s^{-1} $\lesssim v_{\rm circ} \lesssim 93$ km s^{-1}. More recently, Dijkstra et al. (2004) found that such a suppression is likely to be countered by strong self-shielding for $z \gtrsim 3$. For concreteness, we completely suppress star formation in halos with $T_{\rm vir} < 10^4$ K for $z < 7$ (assumed to correspond to the redshift of reionization, when the background radiation is established; e.g., Mesinger & Haiman 2004) and increase the cutoff to $v_{\rm circ} < 55$ km s^{-1} ($T_{\rm vir} < 1.1 \times 10^5$ K) for $z < 3$ (when the intermediate halos with 10 km s^{-1} $< v_{\rm circ} <$ 55 km s^{-1} are assumed to cease self-shielding). As can be seen in Figure 4, these assumptions only weakly affect our results, because most of the contribution to $\dot{\rho}_*(z)$ at these redshifts comes from more massive halos. Furthermore, we already bracket a large range of expected GRB distributions by presenting results for both $T_{\rm vir} > 10^4$ K and $T_{\rm vir} > 300$ K.

Finally, we describe two different functional forms for the stellar formation probability density $P(\tau)$.

3.1.1. *Instantaneous Star Formation*

The simplest assumption is to adopt $P(\tau)$ to be a Dirac delta function,

$$P(\tau) = \delta(\tau). \tag{11}$$

This essentially assumes that a fraction $\epsilon_*(\Omega_b/\Omega_M)$ of the currently virializing mass is instantaneously converted into stars and that previously virialized mass does not contribute to $\dot{\rho}_*(z)$. With this assumption, equation (10) becomes

$$\dot{\rho}_*(z) = \epsilon_* \frac{\Omega_b}{\Omega_M} \int_{M_{\rm min}}^{\infty} M \frac{dz}{dt} \frac{\partial^2 n(>M, z)}{\partial z\, \partial M}\, dM. \tag{12}$$

Since the WDM mass functions are obtained with computationally expensive Monte Carlo simulations, we only present their results for this simple model; results for mass functions incorporating a power-spectrum cutoff are presented for both $P(\tau)$ models. In numerically calculating derivatives of the mass functions in WDM [$\Delta n(>M, z)/\Delta z$], we use z step sizes of $\Delta z \sim$ 0.2–0.5 [at high redshifts $\Delta n(>M, z)/\Delta z$ is a flatter function of z, so good accuracy can be achieved even with a larger Δz step size]. The resulting SFR densities are shown in the top left panel of Figure 4. The solid curves assume $T_{\rm vir} > 10^4$ K and include only the effect of the power-spectrum cutoff, assuming cutoff scales of $R_c = 0$ Mpc ($m_x \to \infty$; i.e., standard CDM), $R_c = 0.193$ Mpc ($m_x = 1$ keV), and $R_c = 0.087$ Mpc ($m_x =$ 2 keV) (*top to bottom*). The dashed curves assume $T_{\rm vir} >$ 300 K, with the same cutoff scales. The dotted lines include the additional effect of the effective pressure of WDM particles with a mass of $m_x = 2$ keV and $m_x = 1$ keV (*top to bottom*). Since power is strongly suppressed on scales in excess of $T_{\rm vir} >$ 10^4 K for these WDM particle masses cutoff scales, results for $T_{\rm vir} > 10^4$ K and $T_{\rm vir} > 300$ K are virtually the same. In CDM models, the range of virial temperatures result in a wider range of expected SFR densities, highlighted by the shaded area. Our results are within the uncertainties of existing observational estimates of the SFR density in the currently available, low-redshift ($z \lesssim 2$) regime (e.g., Schiminovich et al. 2005). Our SFR density increases out to $z \gtrsim 6$ (and to still higher redshift in the $T_{\rm vir} > 300$ K case) and is consistent with recent estimates at $2 \lesssim z \lesssim 6$ from the Hubble Ultra Deep Field (Bunker et al. 2004), the GOODS surveys (Giavalisco et al. 2004), and the FORS Deep Field on the VLT (Gabasch et al. 2004), after they incorporate a factor of 5–10 increase in the SFR (Adelberger & Steidel 2000) due to dust obscuration. Note that the peak of the SFR density falls between $3 \lesssim z \lesssim 12$ in our range of models and that the SFR remains significant (exceeding its present-day value) out to redshifts as high as $z \gtrsim 25$.

We stress that instant star formation is the most conservative model in setting observational limits to a power-spectrum cutoff, as it predicts the largest number of high-redshift GRB detections. Any other, more realistic form for the stellar formation probability density, $P(\tau)$, delays GRB events, thereby smearing the event rate toward lower redshifts and decreasing the likelihood of detecting high-redshift GRBs, especially in the presence of small-scale power suppression (see § 4.1).

3.1.2. *Exponential Approximation for P(τ)*

We alternatively assume that stellar formation occurs on a timescale corresponding to the dynamical time, $t_{\rm dyn} \sim (G\rho)^{-1/2}$ (Cen & Ostriker 1992; Gnedin 1996):

$$P[t(z) - t(z')] = \frac{t(z) - t(z')}{t_{\rm dyn}^2} \exp\left[-\frac{t(z) - t(z')}{t_{\rm dyn}}\right], \tag{13}$$

where $\rho(z) \approx \Delta_c \rho_{\rm crit}(z)$ is the mean mass density interior to collapsed spherical halos (e.g., Barkana & Loeb 2001), and Δ_c is obtained from the fitting formula in Bryan & Norman (1998), with $\Delta_c = 18\pi^2 \approx 178$ in the Einstein–de Sitter model.

Since there is no unique, physically motivated, and self-consistent way to track individual mass elements and halo mergers in the EPS formalism, assigning an age, $\tau \equiv t(z) - t(z')$, to each mass element is somewhat arbitrary. The problem arises because two neighboring mass elements that are part of the same halo can in EPS be flagged as belonging to two different halos with different masses (Somerville & Kolatt 1999; see also Sheth & Pitman 1997 and Benson et al. 2005). Here we assume that a mass element "starts its clock" ($\tau = 0$) when it first becomes part of a halo with mass $M > M_{\rm min}$ and that it carries around that clock through any future mergers without resetting it. This ambiguity is bypassed in § 3.1.1, since $P(\tau)$ is assumed to be a delta function.

We present our SFR densities for this model in the top right panel of Figure 4. The curves correspond to the same models as shown in the top left panel, except the WDM models with pressure (*dotted curves*) are not included. As expected, introducing a finite width to the stellar formation probability density preferentially suppresses high-redshift star formation.

We remark that the sharp drop at $z = 7$ in the $T_{\rm vir} > 300$ K, CDM curve is an indicator of the assumed sudden reionization (Bromm & Loeb 2002; Choudhury & Srianand 2002). This feature is a direct prediction of reionization models and is indeed likely to be sharp (see, for example, Cen & McDonald [2002] for a discussion, as well as a claim of having detected a related feature in the Lyα transmission spectrum of distant quasars). Given a sufficient number of GRBs, the shape and location of such a feature can be mapped out and used as a probe of the epoch of reionization. We postpone a detailed exploration of the detectability of such a feature to a future paper.

3.2. *The GRB Rate Associated with Star Formation*

In order to constrain the proportionality constant K by matching the predicted and observed GRB rates, a luminosity function (LF) for the GRB population needs to be assumed. Observations have shown that GRBs are far from being standard candles (and even if the total GRB energy has a nearly universal value, the burst luminosity will vary; Frail et al. 2001). However, the determination of their intrinsic LF has been hampered so far by the lack of a sufficiently large sample with detected redshifts. On the other hand, fits to the observed flux distribution suffer from a degeneracy between the LF and the SFR that prevents an independent determination of both quantities.

On the theoretical side, simulations of jets in the collapsar model (MacFadyen & Woosley 1999) have shown that the jet energy (and hence luminosity) is a decreasing function of the viewing angle θ relative to the jet axis, triggering studies of structured jets (Rossi et al. 2002; Zhang & Mészáros 2002). Here, following Rossi et al. (2002), we assume that the luminosity has a form $L = L_{\rm min}(\theta_{\rm jet}/\theta)^2$ for $\theta_{\rm core} < \theta < \theta_{\rm jet}$, where $\theta_{\rm core}$ defines the core of the jet (within which the luminosity is constant), and $\theta_{\rm jet}$ defines the outer edge of the jet (above which the luminosity drops to zero). Current observations have shown that $\theta_{\rm core} \lesssim 0.06$ rad and $\theta_{\rm jet} \gtrsim 0.6$ rad (Bloom et al. 2003). Our results are insensitive to the precise value of $\theta_{\rm core}$ below the observed minimum value, and therefore we set it to zero for simplicity. The GRB rate at $z = 0$ is, however, dependent on $\theta_{\rm jet}$ (or equivalently, the inferred minimum luminosity $L_{\rm min}$; see also Guetta et al. 2004).

For each of the models for the SFR described in the previous section, we determine the constant $L_{\rm min}$ by finding the best fit between the theoretical and the observed flux distribution of bursts (unnormalized; i.e., using only the shapes of the distributions). In this fitting procedure, we fix the jet angle to be $\theta_{\rm jet} = \pi/2$ (but consider the alternative $\theta_{\rm jet} = 0.6$ rad, the lowest value directly inferred from observations so far; see below). In practice, a distribution of viewing angles is inferred for the theoretical GRBs (assuming random jet orientations) and compared to the distribution $dn/d\theta$ inferred from the bursts detected by BATSE (see Perna et al. [2003] for details of the analysis). The proportionality constant K is then separately determined by imposing that the total number of bursts $\int_0^{\pi/2} d\theta(dn/d\theta)$ above the BATSE sensitivity ($\sim$0.25 ph s^{-1} cm^{-2}) be 667 yr^{-1}. Once these two model parameters are determined, the number of bursts observed at redshifts greater than z over a time interval $\Delta t_{\rm obs}$ and solid angle $\Delta\Omega$,

$$N(>z) = \frac{\Delta\Omega}{4\pi}\Delta t_{\rm obs}\int_z^\infty dz'\,\frac{\dot{\rho}_{\rm GRB}(z')}{(1+z')}\frac{dV(z')}{dz'}\int_0^{\theta_{\rm max}(z')} P(\theta)\,d\theta, \qquad (14)$$

can be found for the *Swift* sensitivity ($F_{\rm lim} \sim 0.04$ ph s^{-1} cm^{-2}). We adopt a solid angle $\Delta\Omega = 0.34$ sr, for the fully coded detector area of *Swift*. In the above equation $P(\theta)d\theta = \sin\theta d\theta$ is the probability of viewing a randomly oriented GRB at an angle from the jet axis between θ and $\theta + d\theta$, the factor $1/(1+z)$ accounts for time dilation, and $dV(z)/dz$ is the comoving volume in our past light cone per unit redshift,

$$\frac{dV(z)}{dz} = 4\pi c\frac{d_L^2(z)}{1+z}\left|\frac{dt}{dz}\right|, \qquad (15)$$

where c is the speed of light, and $d_L(z)$ is the luminosity distance. The maximum angle $\theta_{\rm max}$ at which a burst can be detected at a given redshift is found by numerically inverting the equation

$$F_{\rm lim} = \frac{L(\theta_{\rm max})}{4\pi d_L^2(z)(1+z)^\alpha}, \qquad (16)$$

where α is the power-law spectral index of the photon number spectrum of the burst (see Lamb & Reichart [2000] for details).

For illustration, in Figure 5, we show the fraction of all bursts at redshift z that would be detectable by BATSE (*dashed curves*) and by *Swift* (*solid curves*). The lower/upper curves correspond to jet angles of $\theta_{\rm jet} = \pi/2$ and 0.6 rad, respectively. In our fiducial model, *Swift* detects all GRBs out to $z \sim 1$ and $\sim$1% of GRBs at $z \sim 10$.

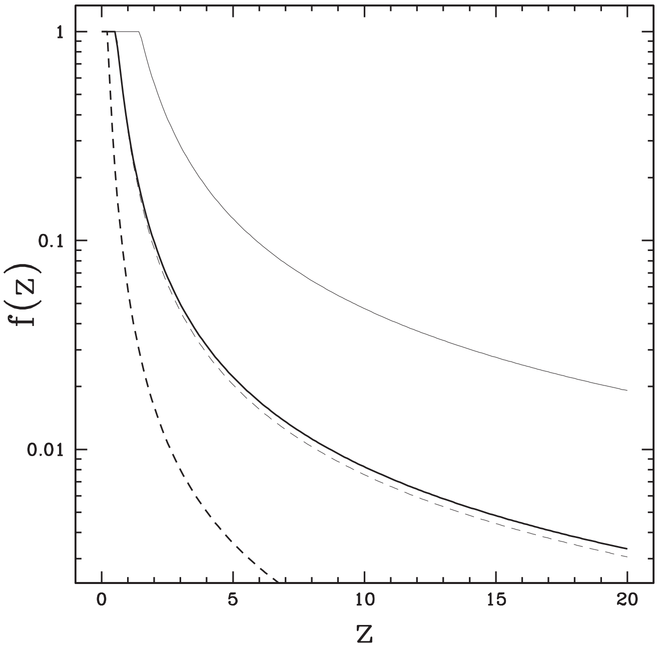

Fig. 5.—Fraction of all GRBs that are brighter in our model luminosity function than the detection thresholds of BATSE (*dashed curves*) and *Swift* (*solid curves*). The lower/upper curve in both cases corresponds to jet angles of $\theta_{\rm jet} = \pi/2$ and 0.6 rad, respectively. In each case, we determine the minimum burst luminosity $L_{\rm min}$ so that the flux distribution predicted in our CDM model with a threshold virial temperature $T_{\rm vir} = 10^4$ K best fits the distribution observed by BATSE.

The value of the normalization constant K, inferred from the BATSE data, is dependent on the value of $L_{\rm min}$. For example, in the CDM models with instantaneous star formation and $T_{\rm vir} > 10^4$ K, for our fiducial choice of $\theta_{\rm jet} = \pi/2$, we find the best-fitting value of $L_{\rm min} = 1.5 \times 10^{55}$ ph s^{-1} and the local GRB rate of $\dot{\rho}_{\rm GRB}(z=0) = 6$ Gpc^{-3} yr^{-1}, while for $\theta_{\rm jet} = 0.6$ rad, we find instead $L_{\rm min} = 10^{56}$ ph s^{-1} and $\dot{\rho}_{\rm GRB}(z=0) = 1$ Gpc^{-3} yr^{-1}.

Nevertheless, we find that our subsequent predictions for the number of bursts at high redshift by *Swift* are only mildly dependent on the choice of $\theta_{\rm jet}$. This is because as $L_{\rm min}$ is increased, the normalization factor K decreases. This tends to compensate for the increase in the observable number of bursts because there is a larger fraction of bursts at higher luminosities. As can be seen in Figure 5, at high redshift only the bright power-law tail of GRBs are detectable, and the two effects nearly cancel. We note that the slope of $N(>z)$ depends on the power-law slope of the LF. Our model has $dn/dL \propto L^{-\gamma}$, with $\gamma = 2$ in the high-luminosity tail—for comparison, by fitting a single power law to dn/dL, Firmani et al. (2004) find a shallower slope, with $\gamma \sim 1.6$. If this slope is accurate for high luminosities, it would somewhat increase the number of high-z GRBs. Of course, once *Swift* data have been gathered, they will provide new and independent constraints on the GRB luminosity function, facilitating more accurate estimates of the high-z GRB rate.

3.3. *Uncertainties in GRB Redshift Evolution*

Our most important model assumptions are that ϵ_* and K are constant. Observations of nearby dwarf galaxies (Taylor et al. 1999; Walter et al. 2001) yield a range of efficiencies, $\epsilon_* \approx 0.02$–0.08. These values correspond to the low halo mass scales that form at high redshifts, although there is no clear direct correspondence between the first-generation halos and these local dwarfs. Numerical simulations of metal-free star formation at high redshift (Abel et al. 2002; Bromm et al. 2002) suggest that the first generation of stars form in minihalos with even lower efficiencies, $\epsilon_* \lesssim 0.01$. Such a reduction in minihalo star formation ($T_{\rm vir} < 10^4$ K) suggests that at high redshifts, the true GRB rate is closer to our $T_{\rm vir} > 10^4$ K curve.

On the other hand, since GRB progenitors involve high-mass stars (MacFadyen & Woosley 1999), and the stellar initial mass function (IMF) is expected to be more top heavy in the early universe, K might increase at high redshifts, increasing $\dot{\rho}_{\rm GRB}(z)$. We note that the minimum mass of stars that lose their hydrogen envelope and may thus produce GRBs can also strongly depend on metallicity. Heger et al. (2003) find that this minimum mass increases from $\approx 30\ M_\odot$ at solar metallicity to $\approx 100\ M_\odot$ at zero metallicity (see their Fig. 3). However, the trend is still more likely to be for K to increase toward high redshift, because $>30\ M_\odot$ stars are relatively rare in local galaxies with a Salpeter IMF, while the simulations of Abel et al. (2002) and Bromm et al. (2002) suggest that metal-free star formation at high redshift may produce exclusively $>100\ M_\odot$ stars. Thus, since they are expected to act in opposite directions, the redshift evolutions of ϵ_* and K might compensate somewhat for each other. The rather high angular momentum of the collapsing star required to produce a GRB is more easily achieved if the star is in a binary, and binaries are found to be more frequent at low metallicity (i.e., high z; Fryer et al. 1999). It is, however, unclear whether binaries do form in the first generation of truly metal-free halos. Simulations following direct cosmological initial conditions by Abel et al. (2002) find a single star with no further fragmentation; however, different simulations with somewhat more artificial initial conditions (a rotating cylinder) find efficient binary formation (Saigo et al. 2004).

It is conceivable that at high redshifts, a WDM universe could mimic the GRB rates of a CDM universe by compensating for a loss of small-scale power with higher efficiencies of GRB production (e.g., a higher K value at high redshifts) and visa versa. However, we note that such a redshift evolution is unlikely to be sharp enough to significantly affect our conclusions. Even a power-law evolution of K would be insufficient to compensate for the exponential suppression of small-scale power in our models. For example, from Figure 6 we note that in order for GRB rates in WDM models with $m_x \approx 2$ keV to match GRB rates in CDM models at $z > 10$, the product $\epsilon_* K$ would need to be a factor of 10 higher than the overall average value determined from the lower redshift BATSE sample. For $m_x \approx 1$ keV, $\epsilon_* K$ would have to be ~ 100 times larger at $z > 10$. These differences only increase with increasing redshift, and if such an increase is present, it could, in principle, be detected by studying the *shape* of the GRB redshift distribution function (see § 4.2).

Recently, Wise & Abel (2004) calculated primordial supernovae (SNe) rates with a semianalytic analysis of feedback mechanisms and evolution of primordial stellar environments, constraining their results with the measured *WMAP* optical depth to electron scattering, $\tau_e = 0.17$. With ab initio knowledge of GRB progenitors, an analogous analysis could be performed to predict the GRB rate as a function of redshift, replacing the proportionality constant, K, assumed in this paper. In practice, our current knowledge of the physics of GRB progenitors and of the various feedback processes in the early universe is highly uncertain, and such an approach would introduce additional free parameters. Nevertheless, this approach could be useful in the future, since some of the free parameters may be independently constrained. For example, in addition to GRBs, early star formation will be accompanied by observable SN explosions (e.g., Miralda-Escudé & Rees 1997), the production of heavy elements (e.g., Haiman & Loeb 1997), remnant stellar black holes (e.g., Volonteri et al. 2003; Volonteri & Perna 2005), and the reionization of the IGM. Observations of these effects can further reduce the uncertainties associated with early star formation history and GRB progenitors, and thus ultimately reduce uncertainties on the expected primordial GRB event rates (for a discussion of such future constraints, see Wise & Abel [2004], who also emphasize that SNe observations can constrain many properties, such as mass, luminosity, metallicity, and redshift, of the progenitors). Finally, early "minigalaxies" may also be directly detectable (Haiman & Loeb 1997) by the *James Webb Space Telescope*.[2]

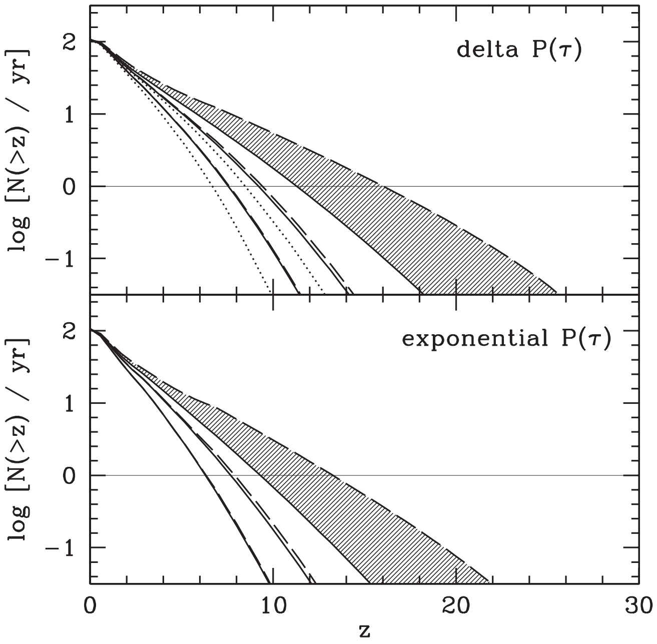

FIG. 6.—Expected *Swift* detection rates of GRBs occurring at redshifts greater than z. The curves correspond to the same models as shown in Fig. 4, and the horizontal line denotes the detection threshold of one GRB yr^{-1}. The top panel assumes instantaneous star formation; the bottom panel assumes a finite exponential spread in star formation times.

4. CONSTRAINTS ON STRUCTURE FORMATION MODELS

The model outlined in the previous sections can be used to compute the evolution of the GRB rate with redshift, as well as the flux distribution of the bursts, allowing us to incorporate the detection threshold of *Swift*. In this section, we present constraints on WDM models, first from the total number of GRBs, and then we present a potentially less model-dependent constraint from the distribution of a *luminosity-limited* subsample of the bursts.

4.1. *Absolute GRB Detection Rates*

The most straightforward constraints follow from the total *Swift* burst detection rates. In Figure 6, we show the cumulative *Swift* GRB detection rates produced by our models. The curves correspond to the same models as shown in Figure 4, with the shaded area enclosing the range of expected distributions in CDM models for different limiting virial temperatures for star formation

---

[2] See http://www.jwst.nasa.gov.

TABLE 1

Redshift in Several WDM Models beyond Which *Swift* Would Detect 1 or 10 GRBs per Year

Model	1 GRB yr^{-1}	10 GRBs yr^{-1}
CDM:		
$T_{\rm vir} > 10^4$ K	$z \gtrsim 9.40$–11.6	$z \gtrsim 4.8$–5.9
$T_{\rm vir} > 300$ K	$z \gtrsim 13.4$–16.0	$z \gtrsim 6.4$–7.6
$P(k)$ suppr:		
$R_c \lesssim 0.193$ Mpc	$z \gtrsim 6.3$–7.5	$z \gtrsim 3.5$–4.3
$R_c \lesssim 0.087$ Mpc	$z \gtrsim 7.8$–9.3	$z \gtrsim 4.2$–5.1
$R_c \lesssim 0.055$ Mpc	$z \gtrsim 8.4$–10	$z \gtrsim 4.5$–5.4
WDM:		
$m_x \gtrsim 1$ keV	$z \gtrsim 6.7$	$z \gtrsim 3.9$
$m_x \gtrsim 2$ keV	$z \gtrsim 8.5$	$z \gtrsim 4.8$
$m_x \gtrsim 3$ keV	$z \gtrsim 9.5$	$z \gtrsim 5.2$

TABLE 2

Redshift in Models with a Red-tilted or Running Scalar Index, Fixed *Swift* GRB Rates (as in Table 1)

Model	1 GRB yr^{-1}	10 GRBs yr^{-1}
Red Tilt (n_s = 0.9)		
$T_{\rm vir} > 10^4$ K	$z \gtrsim 7.7$–9.3	$z \gtrsim 4.1$–5.0
$T_{\rm vir} > 300$ K	$z \gtrsim 10.5$–12.6	$z \gtrsim 4.8$–6.3
$\sigma_8 = 1$ ($T_{\rm vir} > 10^4$ K)	$z \gtrsim 9.1$–11.1	$z \gtrsim 4.8$–5.8
$\sigma_8 = 1$ ($T_{\rm vir} > 300$ K)	$z \gtrsim 12.2$–14.7	$z \gtrsim 5.8$–7.3
Running ($\alpha = -0.05$)		
$T_{\rm vir} > 10^4$ K	$z \gtrsim 7.4$–8.9	$z \gtrsim 4.0$–4.9
$T_{\rm vir} > 300$ K	$z \gtrsim 8.8$–10.5	$z \gtrsim 4.3$–5.4
$\sigma_8 = 1$ ($T_{\rm vir} > 10^4$ K)	$z \gtrsim 8.7$–10.5	$z \gtrsim 4.6$–5.6
$\sigma_8 = 1$ ($T_{\rm vir} > 300$ K)	$z \gtrsim 10.2$–12.3	$z \gtrsim 5.1$–6.4

in early halos. The top panel assumes instantaneous star formation, and the bottom panel assumes a spread of star formation times as discussed above. The horizontal line denotes a detection rate of one GRB yr^{-1}, roughly the lower limit for detections in *Swift*'s 2 year nominal operation.

Figure 6 shows that detections of bursts originating at redshifts larger than $z \sim 15$ are improbable even in CDM models. Constraints on WDM models can be simply read off this figure by noting the redshifts at which the curves corresponding to a given model intersect the horizontal line. For example, for a WDM particle mass of $m_x = 1$ keV, a detection rate of one $z > 7$ GRB yr^{-1} is expected. That number drops to one $z > 8$ GRB per 10 yr, which is unlikely to be detectable. *A detection of a single* $z \gtrsim 10$ *GRB by Swift would rule out models incorporating WDM or equivalent power-spectrum cutoffs of* $m_x \lesssim 2$ keV ($R_c \gtrsim 0.087$ Mpc) *and would therefore significantly improve the existing constraints.*

These constraints on models with an exponential cutoff in the small-scale power spectrum are summarized further in Table 1. The low end of the quoted redshift range in each case in the top five rows corresponds to the exponential star formation, and the high end to instantaneous star formation (the models that include the effective pressure of WDM particles, listed in the bottom three rows, show only the latter). The rightmost column in the table shows the redshifts beyond which 10 GRBs yr^{-1} would be detectable.

The constraints shown in Table 1 have been derived assuming a fixed cosmological model, varying only the cutoff scale for the power spectrum. However, in principle, the effects of the cutoff can be mitigated by changing other parameters. In particular, the GRB rate depends exponentially on the normalization of the power-spectrum σ_8. In order to quantify the robustness of our results, we have recomputed the redshifts corresponding to one and 10 GRBs yr^{-1} in the CDM model with $T_{\rm vir} > 10^4$ K and in the model with the power-spectrum cutoff at $R_c = 0.193$ Mpc but using a high value of $\sigma_8 = 1$ rather than our fiducial choice of $\sigma_8 = 0.85$. We have found that this increases the redshifts by $\Delta z < 2$; in particular, the $R_c = 0.193$ Mpc model could still be ruled out by observing one GRB yr^{-1} at $z \gtrsim 9.7$.

The corresponding constraints in models with a red tilt or a running of the scalar index are summarized in Table 2. Overall, in the CDM model with the more stringent limit of $T_{\rm vir} > 10^4$ K for star formation, the effect of introducing a tilt with $n_s = 0.9$, or a running of the index with $\alpha = dn_s/d\ln k = -0.05$ is comparable to that of the exponential cutoff in the power spectrum due to a $m_x \approx 2$ keV WDM particle: the GRB rate falls below one per year at $z \gtrsim 8$. However, as the table shows, these constraints are less robust than those for WDM. The suppression of the power spectrum is a shallow function of scale, and, unlike in the case of the exponential suppression, the GRB rate can be increased by either a relatively modest change in the normalization σ_8 or by allowing star formation in smaller halos down to $T_{\rm vir} = 300$ K. The table suggests that a detection rate of one GRB yr^{-1} even at $z \gtrsim 14$ cannot be used to distinguish a tilt of $n_s \approx 0.9$ from models with $n_s = 1$ but with a lower $T_{\rm vir} > 300$ K and a higher σ_8. However, a detection rate of one GRB yr^{-1} at $z \gtrsim 10$ would lead to a relatively robust upper limit on the running of the spectral index, $\alpha \gtrsim -0.05$.

4.2. *Redshift Distribution of a Luminosity-Limited Sample*

A method that is less dependent on models of the GRB LF and that could, in principle, discriminate against WDM models and models with a power spectrum cutoff is to construct a redshift distribution of a *luminosity-limited* subsample of the observed bursts. Under the relatively weak assumption that the LF of GRBs does not evolve with redshift (but without any other assumptions about the LF), this redshift distribution would be proportional to the distribution of all bursts. In the bottom panels of Figure 4, we plot the fractional distribution of all bursts,

$$f \equiv \int_z^\infty dz' \frac{\dot\rho_{\rm GRB}(z')}{(1+z')} \frac{dV(z')}{dz'} \left[\int_0^\infty dz' \frac{\dot\rho_{\rm GRB}(z')}{(1+z')} \frac{dV(z')}{dz'} \right]^{-1}. \tag{17}$$

This quantity is then independent of the value of the normalization K and of the shape of the GRB LF discussed above.

Such intrinsic event rate distributions can be constructed by tracking the redshift distribution only for the subset of GRBs above a minimum luminosity that allows one to see them up to a given high redshift and neglecting GRBs that are fainter than this threshold. By construction, all of the remaining GRBs are luminous enough to be detectable up to the chosen redshift and so trace out the intrinsic event rates, f (i.e., independently of the shape of the LF and K). The high sensitivity of *Swift* makes this still a sizable sample. For example, in the case of the standard CDM model, we find that ≈30% of the bursts would still remain by choosing only the ones above the minimum luminosity that allows for their detection up to $z \sim 10$. Likewise, ≈20% of bursts would constitute the sample with the minimum luminosity that allows for their detection up to $z \sim 15$. The bottom panels of Figure 4 reveal that ~50% of these remaining bright

GRBs would be at redshifts $z \gtrsim 5$, where the curves start showing significant deviations from one another. In the CDM case, this would translate to a sample of $\sim$20 high-redshift ($z \gtrsim 5$) GRBs with which to trace out the redshift distribution in the bottom panels of Figure 4.

Finally, we note that even for this high tail of the LF, the efficiency with which ultra–high-redshift GRBs can be identified is likely to be a decreasing function of redshift itself. Although the network of follow-up instruments throughout the globe, combined with the aggressive search of high-z GRBs, is likely to partly compensate for the difficulties of identifying the GRBs at the highest redshifts, such selection effects would still have to be carefully folded in to an analysis of the real data (see, e.g., Gou et al. [2004] for a recent discussion of the detectability of the afterglows of high-redshift GRBs).

5. CONCLUSIONS

We find that high-redshift GRB detections are effective at constraining the small-scale power spectrum of cosmological density fluctuations. Assuming that GRBs trace out the cosmic SFR, we generate expected GRB detection rates for various cosmological models that include suppression of the density fluctuations on small scales. The effects of such suppressions become more notable at high redshifts, where the characteristic collapse scales are smaller. Correspondingly, we are able to obtain strong constrains from high-redshift GRB detections. For example, a *Swift* detection of a single GRB at $z \gtrsim 10$ or of 10 GRBs at $z \gtrsim 5$ would rule out an exponential suppression of the power spectrum on scales below $R_c = 0.09$ Mpc (exemplified by WDM models with a particle mass of $m_x = 2$ keV). Constructing the intrinsic fractional GRB distribution from a luminosity-limited sample would provide additional constraints that are independent of the uncertainties in the normalization between GRB and SFRs and of the uncertainties in the intrinsic luminosity function of GRBs. We find that a detection of one GRB yr^{-1} at $z \gtrsim 12$ also provides an upper limit on the running of the spectral index, $\alpha \gtrsim -0.05$, thus potentially placing constraints on the inflationary potential. The analysis presented here is also applicable to constraining other physically-motivated models that include a suppression of power on small scales, such as decaying charged-particles models (Kamionkowski & Sigurdson 2005).

We thank Tom Abel and Avi Loeb for useful comments. This work was supported in part by the National Science Foundation through grants AST 03-07200 and AST 03-07291 (to Z. H.) and by NASA through grants NNG04GI88G and SWIF03-0000-0033 (to Z. H.) and SWIF03-0020-0058 (to R. P.).

REFERENCES

Abel, T., Bryan, G. L., & Norman, M. L. 2002, Science, 295, 93

Adelberger, K. L., & Steidel, C. C. 2000, ApJ, 544, 218

Barkana, R., Haiman, Z., & Ostriker, J. P. 2001, ApJ, 558, 482 (BHO)

Barkana, R., & Loeb, A. 2001, Phys. Rep., 349, 125

———. 2004, ApJ, 601, 64

Benson, A. J., Kamionkowski, M., & Hassani, S. H. 2005, MNRAS, 357, 847

Bloom, J. S., Frail, D. A., & Kulkarni, S. R. 2003, ApJ, 594, 674

Bloom, J. S., et al. 1999, Nature, 401, 453

Bode, P., Ostriker, J. P., & Turok, N. 2001, ApJ, 556, 93

Bromm, V., Coppi, P. S., & Larson, R. B. 2002, ApJ, 564, 23

Bromm, V., & Loeb, A. 2002, ApJ, 575, 111

Bryan, G. L., & Norman, M. 1998, ApJ, 495, 80

Bunker, A. J., Stanway, E. R., Ellis, R. S., & McMahon, R. G. 2004, MNRAS, 355, 374

Cen, R. 2003, ApJ, 591, L5

Cen, R., & McDonald, P. 2002, ApJ, 570, 457

Cen, R., & Ostriker, J. P. 1992, ApJ, 399, L113

Choudhury, T. R., & Srianand, R. 2002, MNRAS, 336, L27

Ciardi, B., & Loeb, A. 2000, ApJ, 540, 687

Dijkstra, M., et al. 2004, ApJ, 601, 666

Efstathiou, G. 1992, MNRAS, 256, P43

Eisenstein, D. J., & Hu, W. 1999, ApJ, 511, 5

Fan, X., et al. 2003, AJ, 125, 1649

Firmani, C., Avila-Reese, V., Ghisellini, G., & Tutukov, A. V. 2004, ApJ, 611, 1033

Frail, D. A., et al. 2001, ApJ, 562, L55

Fruchter, A. S., et al. 1999, ApJ, 519, L13

Fryer, C. L., Woosley, S. E., & Hartmann, D. H. 1999, ApJ, 526, 152

Gabasch, A., et al. 2004, ApJ, 616, 83

Garnavich, P., et al. 2003, ApJ, 582, 924

Giavalisco, M., et al. 2004, ApJ, 600, L103

Gnedin, N. Y. 1996, ApJ, 456, 1

Goodman, J. 2000, NewA, 5, 103

Gou, L. J., Mészaros, P., Abel, T., & Zhang, B. 2004, ApJ, 604, 508

Guetta, D., Perna, R., Stella, L., & Vietri, M. 2004, ApJ, 615, L73

Haiman, Z., Abel, T., & Rees, M. J. 2000, ApJ, 534, 11

Haiman, Z., Barkana, R., & Ostriker, J. P. 2001, in AIP Conf. Proc. 586, 20th Texas Symposium on Relativistic Astrophysics, ed. J. C. Wheeler & H. Martel (Melville: AIP), 136

Haiman, Z., & Loeb, A. 1997, ApJ, 483, 21

Heger, A., et al. 2003, ApJ, 591, 288

Hjörth, J., et al. 2003, Nature, 423, 847

Hu, W., Barkana, R., & Gruzinov, A. 2000, Phys. Rev. Lett., 85, 1158

Jenkins, A., et al. 2001, MNRAS, 321, 372

Kamionkowski, M., & Sigurdson, K. 2005, Phys. Rev. Lett., submitted (astro-ph/0311486)

Kinney, W. H. 2003, in NATO Advanced Study Institute on Techniques and Concepts of High Energy Physics, preprint (astro-ph/0301448)

Kodaira, K., et al. 2003, PASJ, 55, L17

Kosowsky, A., & Turner, M. S. 1995, Phys. Rev. D, 52, 1739

Lacey, C., & Cole, S. 1993, MNRAS, 262, 627

Lamb, D., & Haiman, Z. 2003, in ASP Conf. Ser. 312, 3rd Rome Workshop on Gamma-Ray Bursts in the Afterglow Era, ed. L. Piro, F. Frontera, N. Masetti, & M. Feroci (San Francisco: ASP), in press (astro-ph/0312502)

Lamb, D. Q., & Reichart, D. E. 2000, ApJ, 536, 1

MacFadyen, A. I., & Woosley, S. E. 1999, ApJ, 524, 262

Mesinger, A., & Haiman, Z. 2004, ApJ, 611, L69

Miralda-Escudé, J. 1998, ApJ, 501, 15

Miralda-Escudé, J., & Rees, M. J. 1997, ApJ, 478, L57

Peebles, P. J. E. 1980, The Large-Scale Structure of the Universe (Princeton: Princeton Univ. Press)

———. 2000, ApJ, 534, L127

Peiris, H., et al. 2003, ApJS, 148, 213

Perna, R., Sari, R., & Frail, D. 2003, ApJ, 594, 379

Press, W. H., & Schechter, P. 1974, ApJ, 187, 425

Rees, M. J. 1986, MNRAS, 218, 25

Rossi, E., Lazzati, D., & Rees, M. 2002, MNRAS, 332, 945

Sasaki, S. 1994, PASJ, 46, 427

Sellwood, J., & Kosowsky, A. 2001, in ASP Conf. Ser. 240, Gas and Galaxy Evolution, ed. J. Hibbard, M. Rupen, & J. van Gorkom (San Francisco: ASP), 311

Schiminovich, D., et al. 2005, ApJ, 619, L47

Sheth, R. K., Mo, H. J., & Tormen, G. 2001, MNRAS, 323, 1

Sheth, R. K., & Pitman, J. 1997, MNRAS, 289, 66

Sheth, R. K., & Tormen, G. 199, MNRAS, 308, 119

Somerville, R. S., Bullock, J. S., & Livio, M. 2003, ApJ, 593, 616

Somerville, R. S., & Kolatt, T. S. 1999, MNRAS, 305, 1

Spergel, D. N., & Steinhardt, P. J. 2000, Phys. Rev. Lett., 84, 3760

Spergel, D. N., et al. 2003, ApJS, 148, 175

Stanek, K. Z., et al. 2003, ApJ, 591, L17

Taylor, C. L., et al. 1999, A&A, 349, 424

Thoul, A. A., & Weinberg, D. H. 1996, ApJ, 465, 608

Totani, T. 1997, ApJ, 486, L71

———. 1999, ApJ, 511, 41

Saigo, K., Matsumoto, T., & Umemura, M. 2004, ApJ, 615, L65

Volonteri, M., Haardt, F., & Madau, P. 2003, ApJ, 582, 559

Volonteri, M., & Perna, R. 2005, MNRAS, in press

Walter, F., et al. 2001, AJ, 121, 727

Wijers, R. A. M. J., et al. 1998, MNRAS, 294, L13

Wise, J. H., & Abel, T. 2004, ApJ, submitted (astro-ph/0411558)

Zhang, B., & Mészáros, P. 2002, ApJ, 566, 712